Submitted to *Communications Earth & Environment*

The unexpectedly short Holocene Humid Period in Northern Arabia

Ina Neugebauer[1,2], Michèle Dinies[3,4], Birgit Plessen[1], Nadine Dräger[1], Achim Brauer[1], Helmut Brückner[5], Peter Frenzel[6], Gerd Gleixner[7], Philipp Hoelzmann[4], Kim J. Krahn[8], Anna Pint[6], Valérie F. Schwab[7], Anja Schwarz[8], Rik Tjallingii[1] and Max Engel[9,10,*]

1 GFZ German Research Centre for Geosciences, Section Climate Dynamics and Landscape Evolution, Telegrafenberg, 14473 Potsdam, Germany

2 University of Geneva, Department of Earth Sciences, Rue des Maraichers 13, 1205 Genève, Switzerland

3 German Archaeological Institute (DAI), Scientific Department of the Head Office, Im Dol 2–6, 14195 Berlin, Germany

4 Freie Universität Berlin, Institute of Geographical Sciences, Malteser Str. 74-100, 12249 Berlin, Germany

5 University of Cologne, Institute of Geography, Zülpicher Str. 45, 50674 Köln, Germany

6 Friedrich Schiller University Jena, Institute of Earth Sciences, Burgweg 11, 07749 Jena, Germany

7 Max Planck Institute for Biogeochemistry, Research Group Molecular Biogeochemistry, Hans-Knöll-Str. 10, 07745 Jena, Germany

8 Technische Universität Braunschweig, Institute of Geosystems and Bioindication, Langer Kamp 19c, 38106 Braunschweig, Germany

9 Heidelberg University, Institute of Geography, Im Neuenheimer Feld 348, 69120 Heidelberg, Germany

10 Royal Belgian Institute of Natural Sciences, Geological Survey of Belgium, Jennerstraat 13, 1000 Brussels, Belgium

* Corresponding author: Max Engel, max.engel@uni-heidelberg.de

Abstract

The early to middle Holocene Humid Period (HHP) was the last time when precession-forced intensification of summer monsoons and northward migration of associated rainfalls led to a greening of today's arid Saharo-Arabian desert belt. While this wet phase is well confined in N Africa and the S Arabian Peninsula, robust evidence from N Arabia is lacking. Here, we fill this gap with unprecedented annually to sub-decadally resolved proxy data from Tayma, the only known varved lake sediments in N Arabia. Based on stable isotopes, micro-facies analyses and precise varve and radiocarbon dating we distinguish five phases of lake development and prove that the wet phase in N Arabia from 8,800–7,900 years BP is considerably shorter than the commonly defined HHP (11,000–5,500 years BP). Moreover, we find a two century-long peak humidity at Tayma at times when a centennial-scale dry anomaly around 8,200 years BP interrupted the HHP in adjacent regions. This regional disparity is explained by an increased frequency of tropical plumes reaching N Arabia and compensating for the weakened monsoons and/or winter rains. This peak humidity possibly favoured Neolithic migrations into N Arabia indicating very dynamic human response to environmental changes.

Past millennial-scale pluvial periods are thought to have facilitated human dispersal out of Africa[1–3] by providing 'green corridors' through today's arid Saharo-Arabian desert belt[4–6]. Only recently, the Arabian Peninsula got into the focus of human-climate interaction studies, as it demonstrates high ecological sensitivity to climatic changes and represents the geographic nexus between Africa and Asia[1–3,7,8], while the role of the early to middle Holocene Humid Period (HHP) in Neolithic migrations and cultural progress has also been investigated[9,10]. The recent wave of research in Arabia has fundamentally transformed our perception of Arabian prehistory, including discoveries of Middle Palaeolithic (MIS 5 or even

55 older) sites in Central Arabia[11] or traces of *Homo sapiens* in the Nefud desert at approx. 87
56 ka[8], *i.e.* phases associated with conditions more humid than today[2,6].

57 Climate models suggest that the N African monsoon was the dominant moisture source on the
58 Arabian Peninsula during pluvials[1,12]. Yet, this remains a matter of debate for the N Arabian
59 desert[13–15], as stronger insolation intensified and extended both African summer
60 monsoons[1,2,12,16,17] and Mediterranean winter rains[3,18], the latter being the main source of
61 moisture in this region today. In addition, tropical plumes (TPs), *i.e.* tropical synoptic
62 disturbances conveying water vapour as continuous mid-upper tropospheric cloud bands from
63 the Intertropical Convergence Zone (ITCZ) to >15°N, are known to affect N Arabia during
64 winter and spring[14,19,20]. Higher frequency of such patterns during past pluvials was suggested
65 to have contributed significant rainfall to the Saharo-Arabian desert[14,21,22], even though their
66 past role as a moisture source remains poorly understood.

67 The rich archaeological heritage of Arabia is currently unravelled by major research
68 initiatives[7,10,23] and "potentially thousands of water bodies" have been reconstructed for past
69 pluvials[24], but it is still unknown how these water bodies and human habitats exactly looked
70 like and for how long they existed[14,15]. Only a few climate records are available from
71 speleothems in the wider region, i.e. the Levant[25–27] and S Arabia[28,29]. The entire lack of high-
72 resolution palaeoclimate data from N Arabia leads to an inconsistent picture about the timing
73 and magnitude of the HHP for this culturally important corridor to the Middle East, where some
74 lower-resolution lacustrine records have pointed to more humid conditions during MIS 5 and
75 the early to mid-Holocene[9,30–32].

76 The Tayma palaeolake record[4,33] is the only known high-resolution archive of the HHP in N
77 Arabia providing insights into the early to mid-Holocene hydroclimate variability in
78 unprecedented detail. Today, the 20 km²-sized inland sabkha of Tayma with a 660 km²

hydrological catchment (Fig. 1; Supplementary Figs. 1, 2), located at 27°40'N within the arid desert's interior, receives only scarce rains (on average 45 mm a^{-1}) from Mediterranean winter storms, occasional cross-Saharan tropical plumes or Red Sea cyclones between autumn and spring[14] (Fig. 1). Previous investigations of shoreline deposits (Supplementary Figs. 3–5) and sediment cores from the sabkha basin have proven the existence of a >17 m deep, perennial groundwater-supported lake[15] and the spread of grassland[4] during the early Holocene. The catchment-lake ratio (Fig. 1b; Supplementary Fig. 1b) and the short duration of the peak lake phase[4,15,33] exclude the influence of tectonics on lake-level changes, emphasising the significance of the lake as a palaeoclimate archive that is mainly controlled by rainfall and groundwater inflow. Yet, a precise determination of the lake phases was still missing, preventing a detailed view on the evolution of the palaeolake and the palaeoclimatological implications.

Chronology of the Tayma palaeolake record

The Tayma palaeolake record partly contains annually laminated sediments that were counted under the microscope (see Methods, Fig. 2, Supplementary Fig. 9). The new high-resolution age-depth model integrates AMS radiocarbon ages of pollen concentrates, microscopic varve counting and the independent age of a cryptotephra[34] in a Bayesian model (see Methods, Supplementary Table 1, Supplementary Fig. 7). The floating varve chronology comprising 650 ± 40 couplets is anchored to the radiocarbon age scale and constrains the varved lake phase at Tayma to 8,550–7,900 ± 40 cal varve yr BP (± 90 cal yr BP including the ^{14}C measurement error). A robust time marker is provided by the identification of the central Anatolian 'S1' tephra in the lower part of the record, dated in the Dead Sea record to 8,983 ± 83 cal yr BP[34]. The lacustrine and wetland sediments in the Tayma basin deposited from ca. 9,250 to ca. 4,200 cal yr BP (Supplement Fig. 7).

Groundwater vs. rainfall signal in the Tayma record

Compound-specific hydrogen isotope compositions of plant-wax n-alkanes (δD_{wax}), as well as pore-, rain- and groundwater isotopes ($\delta^{18}O_{water}$ and δD_{water}) trace variations in moisture supply and rainfall amount (Fig. 2, Methods and Supplementary Fig. 8). Stable oxygen and carbon isotope compositions of single primary aragonite laminae ($\delta^{18}O_{arag}$ and $\delta^{13}C_{arag}$) and of bulk carbonates ($\delta^{18}O_{carb}$ and $\delta^{13}C_{carb}$) indicate changing ground- and surface-water inflow, lake-water evaporation and the lake-internal productivity (Fig. 2). These data allow to develop a robust scenario for the evolution of the lake. The most striking finding were minimum δD_{wax} values of about -11‰ δD_p (precipitation) for the shallow lake or wetland phase and significantly lighter values down to -28‰ for the Tayma palaeolake, reflecting higher rainfall between 8,800 and 7,950 cal yr BP due to increased precipitation and a probable amount effect (Methods and Supplement Fig. 8).

Evolution of the Tayma palaeolake

The evolution of the lake can be separated into phases I–V, followed by phases VI (wetland) and VII (sabkha). A basal zone from 9,250–8,800 cal yr BP (lake phase I) represents a shallow lake initiated by increasing rainfall and recharge of the local Saq aquifer, when clastic sediments were deposited in a deflated endorheic basin from a prevailing desert environment[4]. Carbonates precipitated with very high $\delta^{18}O_{carb}$ values of around +11‰ and low $\delta^{13}C_{carb}$ values of around -8‰. At ca. 8,800 cal yr BP (lake phase II), a sharp decrease of $\delta^{18}O_{carb}$ to +8‰, increasing $\delta^{13}C_{carb}$ (Fig. 2) and the *in-situ* deposition of the brackish-water ostracod *Cyprideis torosa* (Fig. 2e) indicate reduced lake-water evaporation and the initial establishment of a shallow, but perennial and increasingly productive water body[35] as a response to wetter conditions. At ca. 8,550 cal yr BP the formation of varves started (Fig. 2; Supplementary Figs. 6, 9), reflecting

126 the onset of a deep (>17 m[15], Supplementary Figs. 3–5) and stratified lake that persisted for a
127 period of 650 ± 40 varve years (lake phases III and IV).

128 From ca. 8,550 to 8,250 cal yr BP (lake phase III), variable but continuously decreasing plant
129 wax $\delta D_{nC29,\ nC31}$ values between -100 and -150‰ indicate a humid period with enhanced
130 seasonality[36,37]. The alternating deposition of dark clay- and organic-rich laminae and white,
131 primary aragonite laminae reflects pronounced wet and dry seasons. The $\delta^{18}O_{carb/arag}$ values
132 generally decrease from +8‰ to +6‰ simultaneously with progressively increasing $\delta^{13}C_{carb}$
133 values from about -6 up to +2‰ towards enhanced lake productivity. The positive excursion of
134 $\delta^{18}O_{carb}$ to >+10‰ centred at ca. 8,400 cal yr BP reflects a decadal- to centennial-scale
135 drawback to even stronger dry-season evaporation, which was compensated by enhanced
136 humidity during the rainy season and groundwater inflow, sufficient to sustain a high lake level
137 and varve formation.

138 From ca. 8,250 to 8,000 cal yr BP (lake phase IV) the highest production rate of organic matter
139 in the lake, annual blooms of planktonic diatoms (mainly *Cyclotella* cf. *choctawhatcheeana*)
140 (Supplementary Figs. 6, 9), greatest abundances of foraminifera, the lowest $\delta D_{nC29,\ nC31}$ values
141 down to -155‰ and weakest dry-season evaporation with lowest $\delta^{18}O_{arag}$ values of +4‰
142 characterize the highest lake stand and most humid period at Tayma during the Holocene. This
143 is supported by the distinct change in varve composition from evaporation-driven aragonite
144 varves to productivity-fuelled diatom-aragonite varves and total organic carbon (TOC) contents
145 of up to 5%. From about 8,200 cal yr BP the $\delta D_{nC29,\ nC31}$ values again start to vary between -
146 140‰ and -100‰, and the $\delta^{18}O_{carb/arag}$ values increase from +4 to +8‰ (Fig. 2e; Supplementary
147 Fig. 6).

148 At ca. 7,950 cal yr BP, ceasing diatom and aragonite laminae and more abundant clastic quartz
149 grains of aeolian origin, as well as the first appearance of gypsum show a rapidly declining lake
150 level (lake phase V). This led to the disappearance of varves within a few decades accompanied

by a sharp reduction in TOC content and a decline of $\delta^{13}C_{carb}$ back to a level comparable to the early shallow-lake phase II, prior to 8,550 cal yr BP. Progressively enriched δD_{wax} values of up to -60‰ and $\delta^{18}O_{carb}$ values towards +12‰ reflect a significant decrease in surface- and groundwater inflow and a strongly increasing evaporation, indicating a gradual end of the humid phase over 100–150 years until ca. 7,800 cal yr BP.

Increasing gypsum precipitation and $\delta^{18}O_{carb}$ rising to +12‰ point to a shrinking lake under an increasingly arid climate between 7,800 and ca. 6,800 cal yr BP, after which wetland conditions set in with TOC levels close to 0 and further increasing aeolian influx (phase VI). Around ca. 4,200 cal yr BP greyish mud is replaced by reddish brown clastics mixed with gypsum (phase VII) (Supplementary Figs. 6, 7), reflecting a further aridisation pulse correlating with a dry event recorded at several sites in the E Mediterranean/Middle East, *e.g.* the N Red Sea[38].

Discussion

Our data support existing low-resolution N Arabian palaeoenvironmental records[9,10,30] but we prove that the HHP in N Arabia was remarkably short, lasting only ca. 650 years from 8,550 to 7,900 cal yr BP. In addition, we observe an intriguing regional hydroclimatic diversity, since the aforementioned peak humidity in N Arabia from 8,550 to 7,900 cal yr BP coincides with a widespread, centennial-scale dry anomaly centred around the 8.2 ka cold event at other low-latitude sites in the N Hemisphere such as the E Mediterranean or S Arabia[39] (Fig. 3). A low-latitude dry period between ca. 8,500 and 7,800 cal yr BP was the most pronounced hydroclimatic drawback of the HHP, evidenced *e.g.* in the desiccation or distinct lowstands of N African lakes[40] and diminished runoff of the Nile River[41], leading to re-oxygenation of the E Mediterranean Sea[42,43] (Fig. 3). Drought conditions mostly resulted from reduced summer-monsoon rainfall[28,29]. However, speleothem records from the Levantine region[25] and marine records from the E Mediterranean suggest that Mediterranean winter rains were reduced as well,

as a result of temporary, meltwater-related deceleration of the North Atlantic thermohaline circulation[39,44] (Fig. 3).

We propose that synoptic-scale patterns, which are scarce today, played a more dominant role in delivering moisture to N Arabia between 8,250 and 8,000 cal yr BP resulting in a humidity peak in this region. We suggest that in particular more frequent tropical plumes (TP) led to a moisture surplus in N Arabia that compensated the reduced monsoonal and Mediterranean winter rains during the centennial dry anomaly related to the 8.2 ka event. In contrast to short and localised convective cells of the Active Red Sea Trough pattern (ARST) triggering flash floods in the southern Levant, TPs promote long-lasting moderate rains and thus more effective moisture over a larger region[19]. We presume that TP formation was favoured by ocean-atmosphere feedbacks during the 'cool poles – dry tropics' anomaly around 8.2 ka: lower sea-surface temperatures in the N Atlantic and Mediterranean Sea promote deeper, southwards penetrating mid-latitude troughs and stronger sub-tropical anticyclones (*i.e.* drier air masses). This leads to an intensification of tropical moisture advection and the sub-tropical jet stream, inducing jet streaks that reach as far as northern tropical W Africa and convey moist air to N Arabia at mid- to upper tropospheric levels[20]. The observed moisture surplus in combination with charged aquifers had distinct short-term impacts on the local environment and probably also on human migration. Vegetation resources[4] and the abundance of prey animals[12] increased and stimulated Neolithic migrations into N Arabia as evidenced by abundant Levant-type Pre-Pottery Neolithic A and B assemblages identified in the N branch of the Nefud desert[9,10].

Acknowledgements

This study is a contribution to the interdisciplinary research project "CLEAR – Holocene CLimatic Events of Northern ARabia" (https://clear2018.wordpress.com/), funded by Deutsche Forschungsgemeinschaft (DFG grants EN977/2-1, PL535/2-1, FR1489/5-1). The CLEAR

project was kindly invited and supported by the Saudi-German Joint Archaeological Project at Tayma, led by Ricardo Eichmann, Arnulf Hausleiter (German Archaeological Institute) and Mohammed H. al-Najem (Museum of Archaeology and Ethnography, Tayma). We are grateful for the research permit issued by the Saudi Commission for Tourism and National Heritage, represented by HRH Prince Sultan bin Salman bin Abdulaziz al-Sa'ud. Further support by Jenny Friedrich (sample preparation), Doreen Noack, Andrea Vieth-Hillebrand (GFZ) (hydrogen isotope measurements), Dieter Berger (GFZ) (preparation of thin sections), Christin Kramer (documentation) and Kirstin Jacobson (language editing) is greatly appreciated.

Author contributions

B.P., I.N., M.E. and P.F. designed the study. M.E., H.B., M.D. and A.P. collected the sediment cores. M.D. and I.N. constructed the age model. I.N., B.P., R.T., P.H. and A.B. contributed the sedimentological and microfacies data. B.P and I.N. contributed stable-isotope data on water and carbonates. N.D., V.F.S. and G.G. contributed the leaf-wax n-alkane data. A.P. and P.F. contributed foraminiferal and ostracod analyses. A.S. and K.J.K. contributed the diatom analysis. I.N., M.E. and B.P. wrote the manuscript. All authors discussed and commented on the manuscript.

Additional information

Data reported here are stored at GFZ Data Services (https://...). Supplementary information is available in the online version of the paper. Reprints and permissions information is available online at www.nature.com/reprints. Correspondence and requests for materials should be addressed to M.E.

Competing interests

The authors declare no competing financial or non-financial interests.

Figure legends

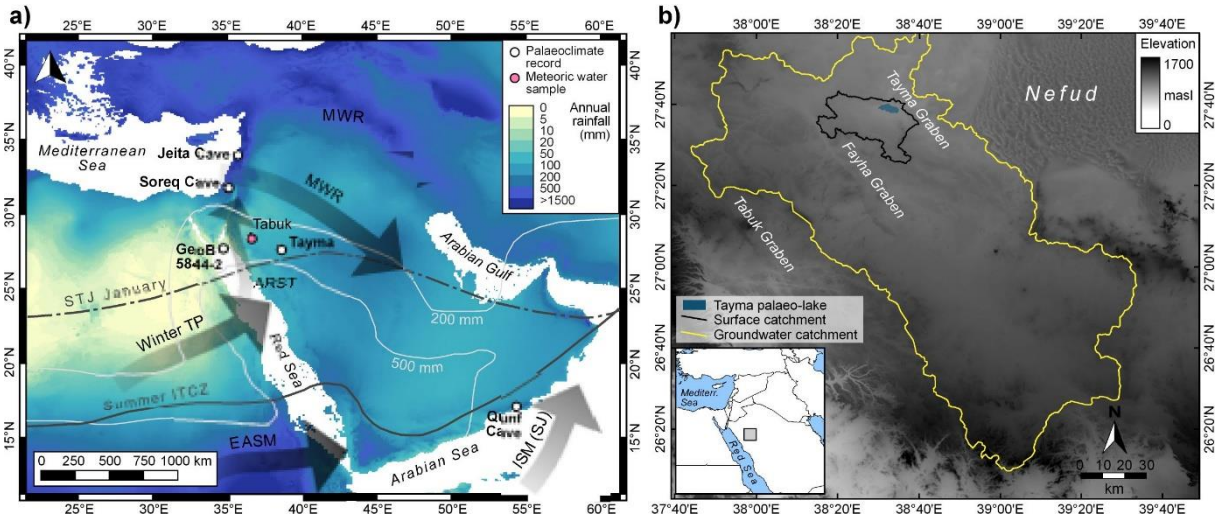

Figure 1: Regional context of Tayma. a) Overview of the Arabian Peninsula and adjacent areas with the key palaeoclimate sites of Jeita Cave[27], Soreq Cave[25,26], GeoB 5844-2 in the Red Sea[13] and Qunf Cave[28], mean annual rainfall 1970–2000 (WorldClim 2 dataset[45]), average positions of the Intertropical Convergence Zone (ITCZ) in summer and the Subtropical Jet (STJ) in winter[46], and atmospheric sources of regional precipitation (MWR = Mediterranean winter rains; Winter TP = Winter tropical plumes; EASM = East African Summer Monsoon; ISM (SJ) = Indian Summer Monsoon (SJ = Somali Jet); ARST = Active Red Sea Trough)[14]. b) Reconstructed extent during the peak phase of the Tayma palaeolake, today's surface catchment and groundwater catchment[47]. The topography is based on GTOPO30 data[48].

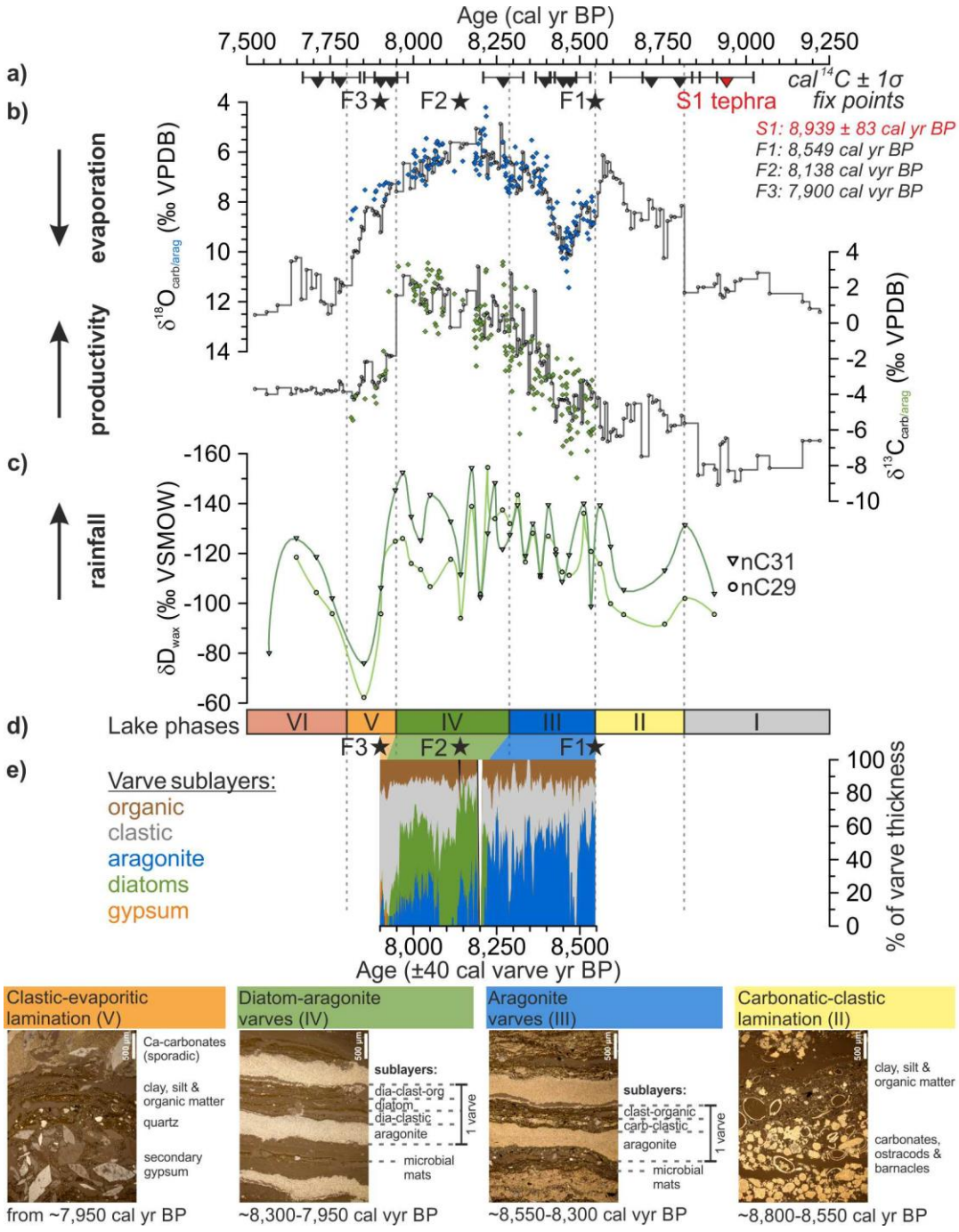

234

235 **Figure 2:** Palaeolake evolution at Tayma between 9,250 and 7,500 cal yr BP. (a) Radiocarbon
236 ages (triangles) and fix points (stars; see Methods); (b) $\delta^{18}O_{carb/arag}$ and $\delta^{13}C_{carb/arag}$ measured on
237 bulk carbonates (solid lines) and on single aragonite layers (blue and green diamonds); (c) δD_{wax}
238 of *n*-alkanes nC_{31} and nC_{29}; (d) Tayma lake phases I–VI; (e) varve sublayers expressed as % of
239 varve thickness for the varve chronology 8,550–7,900 ± 40 cal varve yr BP, and microscope
240 photographs of thin sections highlighting different micro-facies of lake phases II–V.

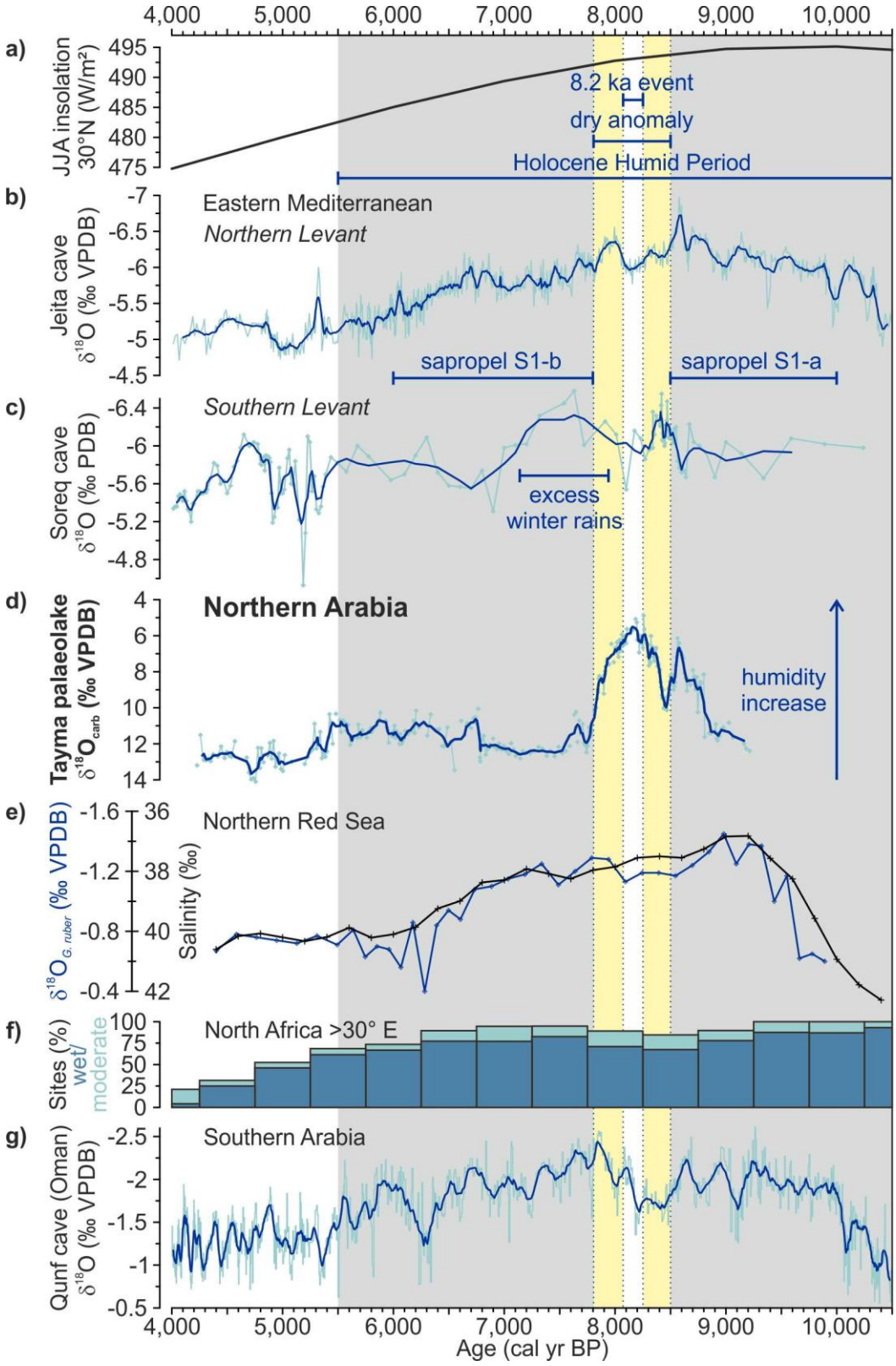

Figure 3: Oxygen isotopes recording humidity changes during the early to middle Holocene Humid Period (HHP) across the E Mediterranean to S Arabia regions. (a) Summer insolation at

245 30°N[49], duration of the HHP[17] (grey), of the low-latitude dry anomaly[39] (yellow), and of the 8.2
246 ka cold event in Greenland ice cores[50] (white bar); (b) speleothem $\delta^{18}O$ from Jeita cave
247 (Lebanon)[27], and (c) Soreq cave (Israel)[25,26], with timing of sapropel formation in the E
248 Mediterranean Sea and winter-rain excess in the S Levant[42]; (d) $\delta^{18}O_{carb}$ from Tayma palaeolake
249 (this study); (e) $\delta^{18}O_{\textit{G. ruber}}$ reflecting temperature, and calculated salinity changes from the N
250 Red Sea[13]; (f) frequency histograms of lake records reflecting wet or moderately wet conditions
251 in the E African monsoon domain >30°E[17]; (g) speleothem $\delta^{18}O$ from Qunf cave (Oman)[28]. All
252 $\delta^{18}O$ scales are reversed to reflect higher humidity upwards.

253

Methods

Tayma sediment cores. Drilling on today's sabkha of the Tayma palaeolake basin was performed in 2011 and 2013 using an Atlas Copco vibracoring device (Cobra mk1) fitted with closed steel auger heads and PVC liners with a diameter of 5 cm. Two series of ca. 6 m long sediment cores (Tay 220/221 and Tay 253/254/255/256) capturing the entire Holocene sequence and reaching down to Ordovician sandstone (Qasim Formation) were obtained in close vicinity ('mastercores' in Supplementary Fig. 1a). They each consist of two parallel, overlapping core sequences A and B with 1 m-long core sections. The cores were opened and photographically documented at the University of Cologne (Laboratory for Physical Geography) and GFZ Potsdam, Germany. The construction of composite profiles and correlation of the sediment cores is based on 24 macroscopic lithological marker layers (fixed marker horizons, FMH).

Tayma sediment cores were analysed for their sedimentology (XRF [X-ray fluorescence] core scanning, quantitative XRF on discrete samples, semi-quantitative XRD [X-ray diffraction], micro-facies analyses on thin sections), geochemistry (elemental analyses, stable isotopes, lipid biomarkers), palynology (vegetation reconstruction through pollen analysis) and micropalaeontology (assemblages of foraminifera, ostracods and diatoms). Here we used stable isotopes of oxygen and carbon ($\delta^{18}O$ and $\delta^{13}C$) measured on primary carbonates in combination with micro-facies analyses of annually laminated (varved) sediments to trace the evolution of the early to mid-Holocene palaeolake at Tayma. Further proxy data have partially been published[4,35,51], or will be presented in forthcoming publications.

In Supplementary Fig. 6, the lithological profile of the ca. 6.5 m-long composite core, TOC (total organic carbon) content[51], $\delta^{18}O_{carb}$ and $\delta^{13}C_{carb}$ (see methodological details further down), and statistical clustering results of the XRF core-scanning record are shown. The elemental composition of the sediment core was determined by non-destructive XRF core scanning on the

split-core sediment surface using an ITRAX elemental scanner at GFZ Potsdam. Measurements were obtained every 0.2 mm using a Cr X-ray source, operated at 30 kV, 30 mA and 10 s, to capture intensities of the elements Si, S, Cl, K, Ca, Ti, Fe, Sr and Zr. A centred log-ratio (clr = ln [element intensity/geometric mean of all nine elements]) transform was performed for all elements of each measurement to eliminate the influences of physical properties, sample geometry and matrix effects[52,53] and to enable robust statistical analyses[54].

The sediments deposited in the Tayma basin are mainly composed of clay, silt and sand, evaporites (sulphates), authigenic carbonates and in parts high amounts of diatoms, ostracods and foraminifera (Supplementary Fig. 6). Clay- and silt-sized detritus is dominant in the core and was deposited as dark grey, mm- to cm-thick, occasionally graded layers. Coarser silt- to sand-sized minerals (mainly quartz) are scattered in the sediments or are concentrated in the uppermost part of the Tayma profile. Evaporites were mainly identified in the form of whitish-beige, finer-grained laminae or post-depositionally grown, large crystals of gypsum and other sulphates. Carbonates are present in the form of white, sub-mm thick primary aragonite laminae, biogenic calcite (ostracods, foraminifera, and barnacle and gastropod shell fragments) and primary magnesium-calcite layers.

Statistical clustering (Ward's method) of XRF core-scanning results indicates four main sediment groups (Supplementary Fig. 6): Cluster 1 (light grey) is dominated by Si, Ti and Fe and describes the siliciclastic sediments and occurs predominantly in the upper part of the Tayma profile (VII – sabkha phase). Cluster 2 (green) does not show a clear preference, but is rather a mixture of all considered elements, describing clastic, carbonate and evaporitic 'background' sediments. Cluster 3 (blue) is dominated by Sr and Ca and describes aragonite, which occurs exclusively in the varved sediments of the Tayma core representing the deep-lake phases III and IV (Fig. 2e). Cluster 4 (orange) is dominated by the elements S and Ca and

303 mainly describes gypsum that was deposited during the terminal lake phase (V) and thereafter,
304 when wetlands occupied the Tayma basin (phase VI).

305 **Varve micro-facies analysis.** We used changes in varve micro-facies, *i.e.* the composition of
306 seasonal sublayers of the annual laminations, to infer changing seasonality and the interannual
307 variability of lake-internal evaporation and productivity. The thickness and composition of
308 varve sublayers were analysed under the microscope along with varve counting on petrographic
309 thin sections. A total of eleven different sublayer types were grouped into five main sediment
310 components (carbonate, organic, clastic, diatoms and gypsum). Data are given as relative
311 contribution (in %) to the varve thickness (Fig. 2e). Raw data of micro-facies sub-layer
312 thicknesses are presented in Supplementary Fig. 9.

313 **Age model construction.** Due to the absence of datable terrestrial macroscopic plant remains
314 in Tayma cores and reported hard-water effects altering radiocarbon ages from gastropods,
315 ostracods and *Ruppia* seeds for up to 1,500 years[4,15], preliminary age models[4,51] were based on
316 AMS radiocarbon dating of pollen grains, as these are unsusceptible for incorporating old
317 carbon[55,56]. Pollen extraction from a total of 33 samples of 1–13 cm long sediment sections
318 followed a combination of physical and chemical separation protocols[55–58]. Sample preparation
319 included sieving (at 6, 20, 40 and 70 µm), treatment with heated HCl, KOH and H_2SO_4, and
320 heavy-liquid density separation using CsCl and sodium polytungstate.

321 Varve counting was performed on 14 large-scale (10 cm x 1.5 cm) petrographic thin sections
322 using a Leica DMLP petrographic microscope under semi-/fully polarised light and with 50x
323 magnification. Thin sections were prepared following standard procedures for soft sediments[59]
324 including freeze-drying and impregnation with epoxy resin (Araldite 2020). Sawing and
325 polishing were performed manually under dry conditions to avoid salt crystallisation. Multiple

counting and the definition of correlation marker layers ensured a negligible subjective counting error. Counting uncertainty due to poor sublayer quality is ± 40 varves (6.2%).

The age-depth model was constructed with Bacon v2.2 using flexible Bayesian modelling[60] including implemented outlier analysis and the IntCal13 atmospheric calibration curve[61]. All 38 radiocarbon ages of pollen concentrates, other plant remains (*Ruppia* seeds, non-pollen palynomorphs, charred plant particles), two mollusc samples, as well as a tephrochronological anchor identified close to the base of the Tayma sediment record (the central Anatolian 'S1'-tephra dated at 8,983 ± 83 cal yr BP in the Dead Sea)[34], were considered for age modelling. The floating varve chronology of 650 ± 40 varve years served to refine the Bayesian model within the varved section. The start of varve formation is defined by ^{14}C dating to 8,549 cal yr BP (8,470–8,605 cal yr BP for the 95.4% probability range). Based on this fix point (F1), the varve age of a turbidite layer at 8,138 ± 40 varve years BP and the end of varve formation at 7,900 ± 40 varve years BP were used as further fix points (F2 and F3) in the adjusted Bayesian model (Supplementary Fig. 7).

Outlier analysis reliably discarded samples (n = 6) containing ≤50% pollen or hard-water-affected material (gastropod shells, *Ruppia* seeds), and 13 samples with ≥50% pollen unsuitable for the Bayesian age-depth model. All remaining 18 ^{14}C ages of pollen concentrates included in the final model contained high pollen concentrations of at least 50% (Supplementary Table 1, Supplementary Fig. 7).

Reconstruction of hydroclimatic conditions. The stable isotope composition of $\delta^{18}O$ and δD of lake water in closed lakes is mainly controlled by precipitation and evaporation and reflects hydrological changes and moisture sources[62]. The $\delta^{18}O_{carb/arag}$ ($\delta^{13}C$) values of lake carbonates and δD_{wax} from fossil leaf waxes in lake sediments are proxies for hydroclimatic conditions and were used to reconstruct the precipitation, lake-water evaporation and temperature during the

early to mid-Holocene. To assess the hydrological balance of the Tayma palaeolake (8,800–7,950 cal yr BP), the wetland (7,800-6,800 cal yr BP), and the potential moisture sources during the HHP, we compared calculated δD_p (precipitation) and $\delta^{18}O_{water}$ (lake water) values with the isotopic characterization of the main regional atmospheric systems, recent precipitation, as well as surface and groundwater isotope compositions (Supplementary Fig. 8).

Stable oxygen and carbon isotope measurements ($\delta^{13}C_{carb}$ and $\delta^{18}O_{carb}$) were performed on the carbonate fraction of a total of 262 freeze-dried and ground samples taken in cm slices from core Tay 220. Bulk samples of ~0.4 mg were loaded into 10 ml Labco Exetainer vials, automatically flushed with He and reacted in phosphoric acid (100%) at 75 °C for 60 min[63]. The stable isotope compositions were determined at GFZ Potsdam using a Finnigan GasBenchII with carbonate option coupled to a DELTAplusXL IRMS (isotope ratio mass spectrometer) (ThermoFisher Scientific). For $\delta^{18}O_{arag}$ and $\delta^{13}C_{arag}$ determination on 165 single aragonite laminae, about 0.06 mg per lamina was taken from dried and impregnated sediment blocks by drilling. For the isotope measurements of ostracods ($\delta^{18}O_{ostr}$ and $\delta^{13}C_{ostr}$), intact valves of adult specimens of *Cyprideis torosa* (Jones, 1850) were hand-picked from the wet-sieved and dried sediment fraction >125 µm. Aragonite and ostracod samples were measured at GFZ Potsdam with an automated carbonate device (KIEL IV) coupled to a Finnigan MAT253 IRMS (ThermoFisher Scientific) on cryogenically purified CO_2 released by dissolution with 103% H_3PO_4 at 72 °C. Oxygen and carbon isotope compositions are given relative to the VPDB (Vienna Peedee Belemnite) standard in conventional delta notation δ (‰). Calibration was performed using international reference standards (NBS18 and NBS19). For both methods, standard deviations (1σ) for reference and replicate analyses are better than 0.08‰ for $\delta^{18}O$ and $\delta^{13}C$.

In closed lakes, $\delta^{18}O_{carb}$ values mainly reflect hydrological changes and are used as a proxy for precipitation, groundwater influx and lake evaporation because: (i) seasonality and temperature

have little effect on oxygen isotope fractionation of precipitation in low-latitude regions[62,64]; (ii) the lake water oxygen isotopic composition in an endorheic basin is governed by evaporation under arid climate conditions resulting in increased $\delta^{18}O_{water}$; (iii) equilibrium oxygen isotope fractionation is assumed for inorganic carbonates; and (iv) primary inorganic carbonates precipitate during the spring-summer season induced by evaporation and/or phytoplankton bloom in the epilimnion. The latter is consistent with increasing $\delta^{13}C_{carb}$ values, indicating ^{12}C depletion of the total dissolved inorganic carbon (TDIC) due to atmospheric release and/or preferential use of aquatic plants.

The calculation of $\delta^{18}O_{VSMOW}$ palaeolake water from the carbonate $\delta^{18}O_{VPDB}$ values using the re-expressed relationship of ref[65] in the simplified eq. (1) according to ref[62]:

(1) $T°C=13.8–4.58(\delta c–\delta w)$

under equilibrium water-calcite precipitation at 21 °C (as average temperature in spring) and an offset of +0.6‰ for aragonite and magnesium bearing calcite reveals comparable $\delta^{18}O$ values between precipitated carbonates and host water. The modelled mean $\delta^{18}O_{water}$ for the palaeolake water is high with +8.4‰ and, thus, significantly lighter due to freshwater inflow of surface and groundwater than for the wetland with a calculated mean $\delta^{18}O_{water}$ of +13.1‰ due to lower precipitation and high evaporation.

Stable hydrogen isotopes of leaf-wax *n*-alkanes (δD_{wax}) were measured on 64 samples from core Tay 255. Samples were taken in 1 cm-slices, freeze-dried and grounded for lipid biomarkers extraction at the Max Planck Institute (MPI) for Biogeochemistry in Jena. 5–15 g of the sample was extracted using a 40 ml dichloromethane:methanol (9:1) mixture at 100 °C and 120 bar for 15 min in two consecutive cycles using a BÜCHI SpeedExtractor. The total lipid extract was separated into aliphatic, aromatic and alcohol/fatty acid fractions using solid-phase extraction on silica gel according to the method presented in ref[66]. The aliphatic

399 hydrocarbon fraction was desulfurized using HCl-activated copper (15% HCl). Identification
400 and quantification of *n*-alkanes were accomplished using a GC-MS (Agilent Technologies,
401 7890A GC-System; 220 Ion trap MS) by comparing peak areas and retention times with an
402 external *n*-alkane standard mixture (*n*C16 to *n*C36). Compound-specific hydrogen isotope
403 ratios (expressed as δD) of the *n*-alkanes were measured on a DELTA V^{plus} Isotope Ratio Mass
404 Spectrometer (IRMS; Thermo Scientific) coupled to an Agilent 7890 GC (Agilent
405 Technologies) at GFZ Potsdam. Every sample was measured in triplicates. The mean standard
406 deviation of all measured samples was 3‰. The δD values were normalized to the Vienna
407 Standard Mean Ocean Water (VSMOW).

408 The changes in δD_{wax} of the lake records are interpreted as indicator for the variability in
409 precipitation, humidity and vegetation type[64,66]. Hydrogen isotopes δD_{wax} of leaf wax nC_{29} and
410 nC_{31} *n*-alkanes were used to calculate δD_p between precipitation (p) according to refs[36,37]. The
411 negative isotopic fractionation from δD_p to δD_{wax} due to the incorporation of hydrogen in leaf
412 waxes has been calculated using eq. (2):

413 (2) $$\delta D_p = [(\delta D_{wax} + 1000)/((\varepsilon/1000)+1)] - 1000$$

414 with ε = -130 for nC_{29} and nC_{31} *n*-alkanes representing the mixture of C3/C4 plant waxes of
415 grasses, shrubs and trees[4] (Supplementary Fig. 8). Following ref[5], we inferred the precipitation
416 rate from δD_p values. The relationship of precipitation and rainfall amount for the Sahara region
417 described a non-linear dependence with a steep slope in δD_p values below 100 mm/a and a
418 strong influence of the amount effect.

419 **$\delta^{18}O$ and δD isotopes of water samples.** Filtered water samples of groundwater from the
420 historical Bir Haddaj well of the Tayma oasis, from the Tay 255 borehole in the palaeolake, and
421 evaporated rainwaters from small water pools south of the palaeolake taken shortly after a rain
422 event in December 2015, were triple-measured for $\delta^{18}O_{water}$ and δD_{water} relative to VSMOW

using Cavity Ring-Down spectrometers (PICARRO L2120-i and L2130-I). Analytical precision of VSMOW and SLAP calibrated analyses was <1‰ for both, $\delta^{18}O_{water}$ and δD_{water}.

The isotopic fractionation of lake-water evaporation was calculated for the remaining lake water ($\delta^{18}O_{rw}$) using initial groundwater-supported lake water with $\delta^{18}O_{iw}$ of -3‰ with simple Rayleigh distillation after eq. (3):

(3) $$\delta^{18}O_{rw}=\delta^{18}O_{iw}-1000(f^{(\alpha-1)}-1)$$

where α = fractionation factor between water and vapor at 21 °C[67] and f = fraction of remaining lake water.

Reconstruction of palaeo-moisture source and lake-water evaporation. The few meteoric water samples from Tabuk (IAEA) plot with $\delta^{18}O$ ~-1‰ closely to the global meteoric water line (GMWL), except for one lighter sample tending more to the Eastern Mediterranean meteoric water line (EMMWL). Recent (12/2015) evaporated rainwater samples collected in water pools in a wadi SW of the Tayma palaeolake show $\delta^{18}O$ values of around -0.5‰ and slightly enriched δD values. Using δD_{wax} to estimate past precipitation rates reveals the lowest values of about -2‰ δD_{water} for the wetland phase and values as low as -28‰ for the palaeolake (Supplementary Fig. 8), indicating higher rainfall amounts between 8,800 and 7,950 cal yr BP due to increasing precipitation and a probable amount effect.

The stable isotopes of the Bir Haddaj well in Tayma reflect subsurface groundwater with -3.5‰ $\delta^{18}O$ and -24.6‰ δD, similar to the middle of the Saq aquifer[68,69]. The water from the palaeolake sampled in 1.5 m depth of the well Tay 255 in 2015 with +7.4‰ $\delta^{18}O$ and +16.2‰ δD probably reflects pore-water isotope composition. The portion of surface-water evaporation along the slope between -3‰ $\delta^{18}O_{iw}$ and the Tay 255 well reaches about 70% for the deep lake phase and

445 >80% for the wetland phase. The isotopic difference between the deep palaeolake and the
446 wetland water is mainly influenced by decreases in precipitation and increasing evaporation.
447 Although the three atmospheric systems affecting the NW Arabian Peninsula (Indian Monsoon,
448 Mediterranean Westerlies and African Monsoon) show isotopic fingerprints with more or less
449 variation and deuterium excess, it is unreasonable to decipher the moisture sources during the
450 time of palaeolake formation due to the determination of precipitation using δD_{wax} and $\delta^{18}O_{carb}$
451 being indirect, as well as associated fractionation effects. In general, the moisture source-related
452 isotope fingerprints over the Arabian Peninsula are masked by strong evaporation, continental
453 and altitude effects, sub-cloud evaporation, moisture recycling and the amount effect[70].
454

455 **References**

456 1. Jennings, R. P. et al. The greening of Arabia: Multiple opportunities for human occupation
457 of the Arabian Peninsula during the Late Pleistocene inferred from an ensemble of climate
458 model simulations. *Quat. Int.* **382**, 181-199 (2015).

459 2. Parton, A. et al. Alluvial fan records from southeast Arabia reveal multiple windows for
460 human dispersal. *Geology* **43**, 295-298 (2015).

461 3. Breeze, P. S. et al. Palaeohydrological corridors for hominin dispersals in the Middle East
462 ~250–70,000 years ago. *Quat. Sci. Rev.* **144**, 155-185 (2016).

463 4. Dinies, M., Plessen, B., Neef, R. & Kürschner, H. When the desert was green: Grassland
464 expansion during the early Holocene in northwestern Arabia. *Quat. Int.* **382**, 293-302 (2015).

465 5. Tierney, J. E., Pausata, F. S. R. & deMenocal, P. B. Rainfall regimes of the Green Sahara.
466 *Sci. Adv.* **3**, e1601503 (2017).

467 6. Nicholson, S. L., Hosfield, R., Groucutt, H. S., Pike, A. W. & Fleitmann, D. Beyond
468 arrows on a map: The dynamics of *Homo sapiens* dispersal and occupation of Arabia during
469 Marine Isotope Stage 5. *J. Anthropol. Archaeol.* **62**, 101269 (2021).

470 7. Armitage, S. J. et al. The southern route "Out of Africa": Evidence for an early expansion
471 of modern humans into Arabia. *Science* **331**, 453-456 (2011).

472 8. Gourcutt H. S. et al. *Homo sapiens* in Arabia by 85,000 years ago. *Nature Ecol. Evol.* **2**,
473 800-809 (2018).

474 9. Crassard, R. et al. Beyond the Levant: First evidence of a Pre-Pottery Neolithic incursion
475 into the Nefud Desert, Saudi Arabia. *PLOS ONE* **8**, e68061 (2013).

476 10. Petraglia, M. D., Groucutt, H. S., Guagnin, M., Breeze, P. S. & Boivin, N. Human
477 responses to climate and ecosystem change in ancient Arabia. *P. Natl. Acad. Sci. USA* **117**,
478 8263-8270 (2020).

11. Crassard, R., Hilbert, Y. H., Preusser, F., Wulf, G. & Schiettecatte, J. Middle Palaeolithic occupations in central Saudi Arabia during MIS 5 and MIS 7: new insights on the origins of the peopling of Arabia. *Archaeol. Anthropol. Sci.* **11**, 3101-3120 (2019).

12. Guagnin, M. et al. Rock art imagery as a proxy for Holocene environmental change: A view from Shuwaymis, NW Saudi Arabia. *Holocene* **26**, 1822-1834 (2016).

13. Arz, H. W., Lamy, F., Pätzold, J., Müller, P. J. & Prins, M. Mediterranean moisture source for an Early-Holocene Humid Period in the northern Red Sea. *Science* **300**, 118-121 (2013).

14. Enzel, Y., Kushnir, Y. & Quade, J. The middle Holocene climatic records from Arabia: Reassessing lacustrine environments, shift of ITCZ in Arabian Sea, and impacts of the southwest Indian and African monsoons. *Global Planet. Change* **129**, 69-91 (2015).

15. Engel, M. et al. Lakes or wetlands? A comment on 'The middle Holocene climatic records from Arabia: Reassessing lacustrine environments, shift of ITCZ in Arabian Sea, and impacts of the southwest Indian and African monsoons' by Enzel et al. *Global Planet. Change* **148**, 258-267 (2017).

16. Kutzbach, J. E. & Liu, Z. Response of the African Monsoon to orbital forcing and ocean feedbacks in the middle Holocene. *Science* **278**, 440-443 (1997).

17. Shanahan, T. M. et al. The time-transgressive termination of the African Humid Period. *Nat. Geosci.* **8**, 140-144 (2015).

18. Kutzbach, J. E., Chen, G., Cheng, H., Edwards, R. L. & Liu, Z. Potential role of winter rainfall in explaining increased moisture in the Mediterranean and Middle East during periods of maximum orbitally-forced insolation seasonality. *Clim. Dyn.* **42**, 1079-1095 (2014).

19. Rubin, S., Ziv, B. & Paldor, N. Tropical plumes over eastern North Africa as a source of rain in the Middle East. *Mon. Weather Rev.* **135**, 4135-4148 (2007).

20. Tubi, A., Dayan, U. & Lensky, I. M. Moisture transport by tropical plumes over the Middle East: a 30-year climatology. *Q. J. Roy. Meteorol. Soc.* **143**, 3165-3176 (2017).

21. Waldmann, N., Torfstein, A. & Stein, M. Northward intrusions of low- and mid-latitude storms across the Saharo-Arabian belt during past interglacials. *Geology* **38**, 567-570 (2010).

22. Skinner, C. B. & Poulsen, C. J. The role of fall season tropical plumes in enhancing Saharan rainfall during the African Humid Period. *Geophys. Res. Lett.* **43**, 349-358 (2016).

23. Hausleiter, A., Eichmann, R. & Al-Najem, M. (eds.). *Taymā' I* (Archaeopress, Oxford, 2018).

24. Breeze, P. S. et al. Remote sensing and GIS techniques for reconstructing Arabian palaeohydrology and identifying archaeological sites. *Quat. Int.* **382**, 98-119 (2015).

25. Bar-Matthews, M., Ayalon, A., Gilmour, M., Matthews, A. & Hawkesworth, C. J. Sea–land oxygen isotopic relationships from planktonic foraminifera and speleothems in the Eastern Mediterranean region and their implication for paleorainfall during interglacial intervals. *Geochim. Cosmochim. Acta* **67**, 3181-3199 (2003).

26. Grant, K. M. et al. Rapid coupling between ice volume and polar temperature over the past 150,000 years. *Nature* **491**, 744-747 (2012).

519 27. Cheng, H. et al. The climate variability in northern Levant over the past 20,000 years.
520 *Geophys. Res. Lett.* **42**, 8641-8650 (2015).

521 28. Fleitmann, D. et al. Holocene ITCZ and Indian monsoon dynamics recorded in
522 stalagmites from Oman and Yemen (Socotra). *Quat. Sci. Rev.* **26**, 170-188 (2007).

523 29. Cheng, H. et al. Timing and structure of the 8.2 kyr B.P. event inferred from $\delta^{18}O$ records
524 of stalagmites from China, Oman, and Brazil. *Geology* **37**, 1007-1010 (2009).

525 30. Schulz, E. & Whitney, J. W. Upper Pleistocene and Holocene lakes in the An Nafud,
526 Saudi Arabia. *Hydrobiologia* **143**, 175-190 (1986).

527 31. Rosenberg, T. M. et al. Middle and Late Pleistocene humid periods recorded in
528 palaeolake deposits of the Nafud desert, Saudi Arabia. *Quat. Sci. Rev.* **70**, 109-123 (2013).

529 32. Zielhofer, C. et al. Climate forcing and shifts in water management on the Northwest
530 Arabian Peninsula (mid-Holocene Rasif wetlands, Saudi Arabia). *Quat. Int.* **473**, 120-140
531 (2018).

532 33. Engel, M. et al. The early Holocene humid period in NW Saudi Arabia – sediments,
533 microfossils and palaeo-hydrological modelling. *Quat. Int.* **266**, 131–141 (2012).

534 34. Neugebauer, I. et al. Implications of S1 tephra findings in Dead Sea and Tayma
535 palaeolake sediments for marine reservoir age estimation and palaeoclimate synchronisation.
536 *Quat. Sci. Rev.* **170**, 269-275 (2017).

537 35. Pint, A. et al. How to discriminate athalassic and marginal marine microfaunas:
538 Foraminifera and other fossils from an early Holocene continental lake in northern Saudi
539 Arabia. *J. Foram. Res.* **47**, 175-187 (2017).

540 36. Sachse, D. et al. Molecular paleohydrology: interpreting the hydrogen-isotopic
541 composition of lipid biomarkers from photosynthesizing organisms. *Annu. Rev. Earth Pl. Sc.*
542 **40**, 221-249 (2012).

543 37. Collins, J. A. et al. Estimating the hydrogen isotopic composition of past precipitation
544 using leaf-waxes from western Africa. *Quat. Sci. Rev.* **65**, 88-101 (2013).

545 38. Arz, H. W., Lamy, F., Pätzold, J. A pronounced dry event recorded around 4.2 ka in brine
546 sediments from the northern Red Sea. *Quat. Res.* **66**, 432-441 (2006).

547 39. Rohling, E. J. & Palike, H. Centennial-scale climate cooling with a sudden cold event
548 around 8,200 years ago. *Nature* **434**, 975-979 (2005).

549 40. Gasse, F. Hydrological changes in the African tropics since the Last Glacial Maximum.
550 *Quat. Sci. Rev.* **19**, 189-211 (2000).

551 41. Blanchet, C. L. et al. High- and low-latitude forcing of the Nile River regime during the
552 Holocene inferred from laminated sediments of the Nile deep-sea fan. *Earth Planet. Sci. Lett.*
553 **364**, 98-110 (2013).

554 42. Rohling, E. J., Marino, G. & Grant, K. M. Mediterranean climate and oceanography, and
555 the periodic development of anoxic events (sapropels). *Earth Sci. Rev.* **143**, 62-97 (2015).

556 43. Tesi, T. et al. Large-scale response of the Eastern Mediterranean thermohaline circulation
557 to African monsoon intensification during sapropel S1 formation. *Quat. Sci. Rev.* **159**, 139-
558 154 (2017).

559 44. Pross, J. et al. Massive perturbation in terrestrial ecosystems of the Eastern Mediterranean
560 region associated with the 8.2 kyr BP climatic event. *Geology* **37**, 887-890 (2009).

561 45. Fick, S. E. & Hijmans, R. J. WorldClim 2: new 1-km spatial resolution climate surfaces
562 for global land areas. *Int. J. Climatol.* **37**, 4302-4315 (2017).

563 46. Akçar, N. & Schlüchter, C. Paleoglaciations in Anatolia: A schematic review and first
564 results. *E&G Quat. Sci. J.* **55**, 102-121 (2005).

565 47. Wellbrock, K., Strauss, M., Külls, C. & Grottker, M. in *Des refuges aux oasis: Vivre en*
566 *milieu aride de la Préhistoire à aujourd'hui. XXXVIIIe rencontres internationales*
567 *d'archéologie et d'histoire d'Antibes* (eds. Purdue, L., Charbonnier, J. & Khalidi, L.) 231-249
568 (Éditions APDCA, 2018).

569 48. Danielson, J. J. & Gesch, D. B. Global multi-resolution terrain elevation data 2010
570 (GMTED2010). *USGS Open-File Rep*. **2011–1073** (2011).

571 49. Laskar, J. et al. A long-term numerical solution for the insolation quantities of the Earth.
572 *Astron. Astrophys.* **428**, 261-285 (2004).

573 50. Thomas, E. R. et al. The 8.2 ka event from Greenland ice cores. *Quat. Sci. Rev.* **26**, 70-81
574 (2007).

575 51. Dinies, M., Neef, R., Plessen, B. & Kürschner, H. in *The Archaeology of North Arabia:*
576 *Oases and Landscapes* (ed. Luciani, M.) 57-78 (Austrian Academy of Sciences Press, 2016).

577 52. Weltje, G. J. & Tjallingii, R. Calibration of XRF core scanners for quantitative
578 geochemical logging of sediment cores: Theory and application. *Earth Planet. Sci. Lett.* **274**,
579 423-438 (2008).

580 53. Weltje, G. J. et al. in *Micro-XRF Studies of Sediment Cores* (eds. Croudace, I. W. &
581 Rothwell R. G.) 507-534 (Springer, Dordrecht, 2015).

582 54. Aitchison, J. The statistical analysis of compositional data. *J. R. Stat. Soc. Ser. B* **44**, 139-
583 160 (1982).

584 55. Brown, T. A., Nelson, D. E., Mathewes, R. W., Vogel, J. S. & Southon, J. R.
585 Radiocarbon dating of pollen by accelerator mass spectrometry. *Quat. Res.* **32**, 205-212
586 (1989).

587 56. Vandergoes, M. J. & Prior, C. A. AMS Dating of pollen concentrates – a methodological
588 study of late Quaternary sediments from South Westland, New Zealand. *Radiocarbon* **45**,
589 479-491 (2003).

590 57. Regnéll, J. & Everitt, E. Preparative centrifugation – a new method for preparing pollen
591 concentrates suitable for radiocarbon dating by AMS. *Veg. Hist. Archaeobot.* **5**, 201-205
592 (1996).

593 58. Nakagawa T. et al. Dense-media separation as a more efficient pollen extraction method
594 for use with organic sediment/deposit samples: comparison with the conventional method.
595 *Boreas* **27**, 15-24 (1998).

596 59. Brauer, A. & Casanova, J. Chronology and depositional processes of the laminated
597 sediment record from Lac d'Annecy, French Alps. *J. Paleolimnol.* **25**, 163-177 (2001).

598 60. Blaauw, M. & Christen, J. A. Flexible paleoclimate age-depth models using an
599 autoregressive gamma process. *Bayesian Anal.* **6**, 457-474 (2011).

600 61. Reimer, P. J. et al. IntCal13 and Marine13 radiocarbon age calibration curves 0–50,000
601 Years cal BP. *Radiocarbon* **55**, 1869-1887 (2013).

602 62. Leng, M. J. & Marshall, J. D. Palaeoclimate interpretation of stable isotope data from
603 lake sediment archives. *Quat. Sci. Rev.* **23**, 811-831 (2004).

604 63. Spötl, C. & Vennemann, T. W. Continuous-flow isotope ratio mass spectrometric
605 analysis of carbonate minerals. *Rapid Comm. Mass Sp.* **17**, 1004-1006 (2003).

606 64. Bowen, G. J. Isoscapes: spatial pattern in isotopic biogeochemistry. *Annu. Rev. Earth Pl.*
607 *Sc.* **38**, 161-187 (2010).

608 65. Kim, S.-T. & O'Neil, J. R. Equilibrium and nonequilibrium oxygen isotope effects in
609 synthetic carbonates. *Geochim. Cosmochim. Acta* **61**, 3461-3475 (1997).

610 66. Sachse, D., Radke, J. & Gleixner, G. δD values of individual n-alkanes from terrestrial
611 plants along a climatic gradient – implications for the sedimentary biomarker record. *Org.*
612 *Geochem.* **37**, 469-483 (2006).

613 67. Horita, J. & Wesolowski, D. J. Liquid-vapor fractionation of oxygen and hydrogen
614 isotopes of water from the freezing to the critical temperature. *Geochim. Cosmochim. Acta* **58**,
615 3425-3437 (1994).

616 68. Al-Sagaby, A. & Moallim, A. Isotopes based assessment of groundwater renewal and
617 related anthropogenic effects in water scarce areas: Sand dunes study in Qasim area, Saudi
618 Arabia. *IAEA-TECDOC* **1246**, 221-229 (2001).

619 69. Alyamani, M. S. Isotopic composition of rainfall and ground-water recharge in the
620 western province of Saudi Arabia. *J. Arid Environ.* **49**, 751-760 (2001).

621 70. Michelsen, N. et al. Isotopic and chemical composition of precipitation in Riyadh, Saudi
622 Arabia. *Chem. Geol.* **413**, 51-62 (2015).